Article

The Self-Actuating Droplet That Can Turn: A Molecular Dynamics Simulation

Yalong Kong [1], Zhigang Liu [1], Lin Guo [1,*] and Yu Qiu [2,*]

1 Energy Research Institute, Qilu University of Technology, Jinan 250014, China
2 School of Energy Science and Engineering, Central South University, Changsha 410083, China
* Correspondence: linguo@sderi.cn (L.G.); yu.qiu@csu.edu.cn (Y.Q.)

Abstract: Water collection remains a fundamental challenge to stable and efficient operation of the solar desalination system. Functional surfaces that can realize self-actuation of droplets have shown great potential in improving droplet dynamics without external energy. Therefore, a surface that can make a droplet move spontaneously along a curve was designed for smart droplet manipulation, and the mechanism of the droplet motion was revealed through molecular dynamics simulations. Influences of the wettability difference between the curved track and the background, the width of curved track, and the temperature were evaluated via simulations. The results show that the surface on which the curved track and the background are both hydrophobic enables a faster actuating velocity of the droplet than the hydrophilic-hydrophobic surface and the hydrophilic-hydrophilic surface. The width of the curved track also affects the actuating velocity of the droplet and increasing the TRACK width can increase the actuating velocity of the droplet. However, actuation of the droplet slows down if the width of the curved track is too large. Overall, the mechanism driving the motion of the droplet along the curve was investigated, which opens new opportunities for the application and manufacturing of water collection in solar desalination.

Keywords: solar desalination; droplet smart manipulation; molecular dynamics simulation

1. Introduction

Solar desalination that utilizes abundantly available solar energy to facilitate seawater evaporation has gained growing attention as promising solutions to the ever-increasing scarcity of freshwater. Water collection, however, remains a fundamental challenge to stable and efficient operation of the solar desalination system. Dropwise condensation is the necessary process of water collection, and the departure of efficient condensates remains a critical bottleneck. Recently, functional surfaces that can realize self-actuation of droplets have been proposed, showing great potential in improving droplet dynamics without external energy. Through long-term evolution and development, animals and plants in nature have inspired and enlightened the design of such functional surfaces. For example, surfaces of rice leaves have self-cleaning properties [1]; cactus thorns [2,3] and cobwebs [4,5] collect water based on the Laplace pressure gradient and the surface energy gradient formed by their surface structures; the micro/nano-composite structures of nepenthes [6,7] optimize and enhance the capillary force in the transportation direction and allow directional motion of water on the surface of nepenthes; Namibian desert beetles [8,9] collect droplets using special hydrophilic spikes on their backs and transfer droplets to their mouths via the hydrophobic areas, which enable these beetles to survive in arid environments.

Scholars also achieved self-propelled motion of droplets by constructing irregular structures [10,11], curvature gradients [12–14], and wettability gradients [15–17] on surfaces, which have been reported in applications such as water collection [18,19], condensation heat transfer [20], liquid pumping [21,22], oil-water separation [23,24], and droplet-based

microfluidics [25–27], etc. For example„ Tang et al. [28] prepared a taper copper (Cu) needle with a wettability gradient that combines the structure gradient and the chemical gradient, which realizes the directional collection of droplets. Based on the integrated physical conical structure and the wettability chemo-gradient, Feng et al. [29] achieved a high-efficiency water collection system. Lin et al. [30] devised an inclined column array, which coordinates with the surface wettability to achieve robust directional transmission of droplets via coordination of multiple gradients and multiple structures on the surface. The above research provides effective methods and strategies for fulfilling the self-actuation of droplets, although it is challenging to design and prepare these one-dimensional (1D) or three-dimensional (3D) structures on surfaces. On the contrary, two-dimensional (2D) surfaces are compatible with modern manufacturing technologies and have been widely applied in various cases [31]. For example, Hou et al. [25] employed the one-step electrodeposition method to impart a wettability gradient to the Cu surface. When placing a droplet on the surface, the droplet can be self-actuated under the wettability gradient. Additionally, patterned hydrophilic-hydrophobic surfaces have also been investigated. Hydrophilic-hydrophobic wedge-shaped patterned surfaces have been prepared in many experimental studies [32–40], and droplets can be self-actuated to move from the narrow to the wide conical end on such surfaces. Zheng et al. [38] and Guan et al. [39] applied lubricating oils on wedge-shaped patterned surfaces to reduce resistance of surfaces to droplets and accelerate the droplet motion. Apart from a single patterned surface, wedge-shaped patterns can also be permutated and combined. Bai et al. [41] designed star-patterned surfaces; Wang et al. [31] constructed wedge-shaped tree structures to realize continuous self-actuation of a large quantity of droplets.

Droplets in the research are always actuated along a linear direction, while how to control self-actuation of droplets along a curve on surfaces has not been reported. The non-linear self-actuation of droplets along a curve is important in lab-on-a-chip, microfluidic devices, and analysis of devices involving biological droplets. The non-linear self-actuation is highly flexible when performing complex, high-precision manipulations of microfluids, which enhances the level of integration of microsystems. The development of computer technology and the maturation of commercial numerical simulation software allows researchers to conduct numerical research into droplets on different surfaces through simulations [42–50]. Through molecular dynamics simulations, Xu et al. [43] studied droplet motion on wedge-shaped structural surfaces combining multiple gradients and explored the influences of different wettability gradients and cone angles thereon. Hao et al. [44] simulated the droplet motion in a wedge groove and found that the different initial locations of droplets in the wedge groove determine the direction of the motion of droplets. Guo et al. [45] conducted numerical research and theoretical analysis on the dynamic behaviors of droplets on a tapering fiber with different cross-sections. Mo et al. [46] simulated the directional motion of nanodroplets on an axially symmetric surface with a curvature gradient. Structural systems with different complexities can be established via molecular dynamics simulations. Experimental research from the microscopic perspective provides theoretical and mechanism support for macroscopic experiments, which reflects the superiority of molecular dynamics simulations.

We are aiming to examine a novel concept of surface design. A functional surface that drives droplet motion along a curve without external energy was designed and explored using a molecular dynamic simulations method. The droplet was driven by virtue of the wettability difference between hydrophilic and hydrophobic areas by molecular dynamics simulation. Influences of different factors including the wettability gradient, the width of curved tracks and the temperatures in relation to the motion characteristics of droplets were estimated. It is expected that this novel functional surface extends droplet manipulation strategies and provides water collection solutions in a solar desalination system.

2. Simulation Method

2.1. Molecular Dynamics Simulation System

Simulation System

To generate the curve track, two rectangular regions were built at first and shown in Figure 1. The x, y, z-coordinates of Block 1 were (-58.8, 98), (-39.2, 196), and (0, 3.92) Å, respectively. The x, y, z-coordinates of Block 2 were (0, 98), (0, 196), and (0, 3.92) Å, respectively. Two cylindrical regions were constructed. The centers of Cylinder 1 and Cylinder 2 were O_1 (0, 78.4) Å and O_2 (0, 74.48) Å, and the radii of Cylinder 1 and Cylinder 2 were 78.4 and 70.56 Å. Then the intersecting region of Block 2 and Cylinder 1 was set as Region 1, and the intersecting region of Block 2 and Cylinder 2 was set as Region 2. Steps to generate the curve track were shown as follows. Copper atoms were built in Block 1and set as type 1. Atoms of Region 1 were deleted. Copper atoms were rebuilt in Region 1, but set as type 2. Atoms in Region 2 were deleted, and copper atoms were created with type 1. Finally, the curve track was obtained and marked in blue in Figure 1. In addition, the curve track and the rest of the background were built with different kinds of atoms, which can be set with different wettability and discussed in the following section. A water cubic box with $50 \times 50 \times 50$ Å^3 was generated at the narrow end of the curve and the centroid thereof was placed above the origin of the coordinates. In this way, the initial configuration of the simulation system was established and shown as Figure 1b.
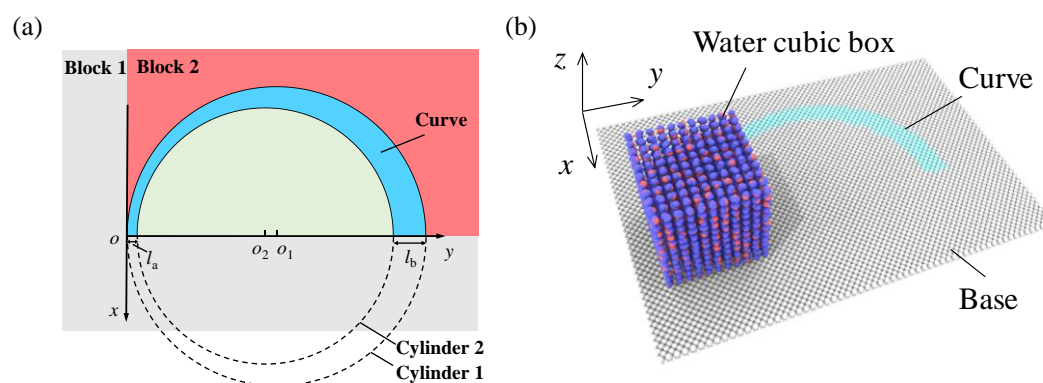
Figure 1. (**a**) Generation of the curve track. (**b**) Initial configuration of the simulation system.

2.2. Simulation Method and Procedure

2.2.1. Simulation Method

Molecular dynamics simulations were adopted to study the self-actuation of droplets along a curve and all simulations were performed using the software package for the large-scale atomic/molecular massively parallel simulator (LAMMPS). The simulation model included water molecules and the copper base. The simulation box measured $180 \times 240 \times 160$ Å and periodic boundary conditions were applied to the x, y, and z-directions. In the whole simulation system, the mixed potential was used as the interaction potential of atomic pairs. The TIP4P model, which was a four-point model, was applied to the water molecule. The quantities of electric charges of oxygen atom and hydrogen atom were -1.0484 e and 0.5242 e, respectively. The bond angle was 104.52°, and the lj/cut/tip4p/long potential model was used for the interaction between atomic pairs in the water molecule.

In the current study, the interactions between copper and copper (Cu-Cu), copper and oxygen (Cu-O), and copper and hydrogen (Cu-H) were described by the Lennard-Jones potential function, shown as follows:

$$E = 4\varepsilon\left[\left(\frac{\sigma}{r}\right)^{12} - \left(\frac{\sigma}{r}\right)^{6}\right] \qquad r < r_{\mathrm{c}} \tag{1}$$

where r represented the interatomic spacing; r_{c} denoted the truncation radius; ε and σ were energy and length parameters, respectively. The energy parameter ε and length

parameter σ of copper-oxygen and copper-hydrogen interactions were calculated based on the Lorentz-Berthelot combining rule. The copper-oxygen interaction strength can be applied to regulate the interfacial wettability, which was determined by the energy coefficient $\varepsilon_{\text{O-Cu}}$ in the current study. The potential energy and relevant parameters used in the simulations were displayed in Table 1.

Table 1. Setting of potential energy parameter.

Inter-Particle Interaction	Type of Potential Energy	Potential Energy Parameter	
		ε/eV	$\sigma/\text{Å}$
O-O	lj/cut/tip4p/long	0.00802	3.1589
O-H	lj/cut/tip4p/long	0	0
H-H	lj/cut/tip4p/long	0	0
Cu-Cu	lj/cut	0.1656	2.471
H-Cu	lj/cut	0	0
O-Cu	lj/cut	Regulation variable	2.815

2.2.2. Simulation Procedure

The canonical ensemble (NVT) was used in the whole simulation during which the initial system temperature was set to 300 K. At first, the simulation system was relaxed for 10 ps, during which all molecules vibrated freely, and the cubic water molecule model took on the shape of a water-drop. The momentum of droplets in the x and y-directions was eliminated and the droplets were only allowed to move along the z-axis, which guaranteed the same initial location of the droplet centroid on the track and complete contact between the droplet and the solid surface. Then, the momentum constraint of the droplet was removed, and the droplet was able to move without additional force. The data acquisition stage was conducted in the microcanonicalensemble (NVE) for 5 ns to study the self-actuation of the droplet along the curve. The simulation data were output every 1000 timesteps, and the droplet trajectories were visualized by the open visualization software OVITO. The droplet velocity was averaged and exported every 5 ps.

2.3. Surface Wettability Simulations

The surface wettability can be defined by the contact angle θ of droplets. The surface was hydrophilic if θ was smaller than 90° and was hydrophobic if θ was greater than 90°. The energy coefficient $\varepsilon_{\text{O-Cu}}$ was applied in the present study to regulate the surface wettability, and the cylindrical droplet method was used to explore the relationship of $\varepsilon_{\text{O-Cu}}$ with the contact angle. Simulation details were shown as follows.

The computation box was $120 \times 120 \times 80$ Å^3 in length. A periodic boundary condition was imposed in the three directions of the computational domain. At first, a water box with 506 water molecules was placed at a prudent distance on top of a copper surface, and the system was allowed to equilibrate. Energy minimization of the system was conducted to remove any excess potential energy from the initial configuration. Then the system was equilibrated using a Nose/Hoover thermostat at 300 K with a time constant of 10 fs for 0.5 ns. After that, equilibration in the microcanonical ensemble with a time step of 10 fs for 0.5 ns was conducted, and snapshots of the system were collected for the next 3 ns.

To extract the profile of the contact line, cylindrical liquid slabs were equilibrated over flat surfaces. Then the microscopic contact angle was like its macroscopic counterpart as predicted by the modified Young equation. The contact angle calculation procedure was as follows: (a) The computational box was discretized into bins of square cross sections in the x–z plane, and the entire length of the computational box in the y direction was the depth of the bins. The resolution of the bins was set as 0.8×0.8 Å^2. The position of each atom of the tested group was stored in the appropriate bin for every snapshot, and the mass density was calculated as the average over time of the bins count per unit volume. (b) The averaged mass density of bins was plotted as contour maps, and the droplet interface was defined by the contour line in which $\rho(x, y) = \rho_l/2$, where ρ_l was the liquid density. (c) The

coordinates of the surface position and the droplet interface are obtained and fitted using the equation of a circle. (d) Finally, the fitted equation was plotted, and the contact angle was measured.

3. Results and Discussion

### 3.1. Effects of Liquid-Solid Interactions on the Contact Angle

The relationship between the potential energy parameters $\varepsilon_{O\text{-}Cu}$ and the θ obtained by simulations was revealed and illustrated in Figure 2. The figure shows that the contact angle decreases as the energy parameter increases, and the surface wettability changes from hydrophobicity to hydrophilicity. Therefore, various contact angle combinations can be set for surfaces with the curve track, which are elaborated in the following investigations.
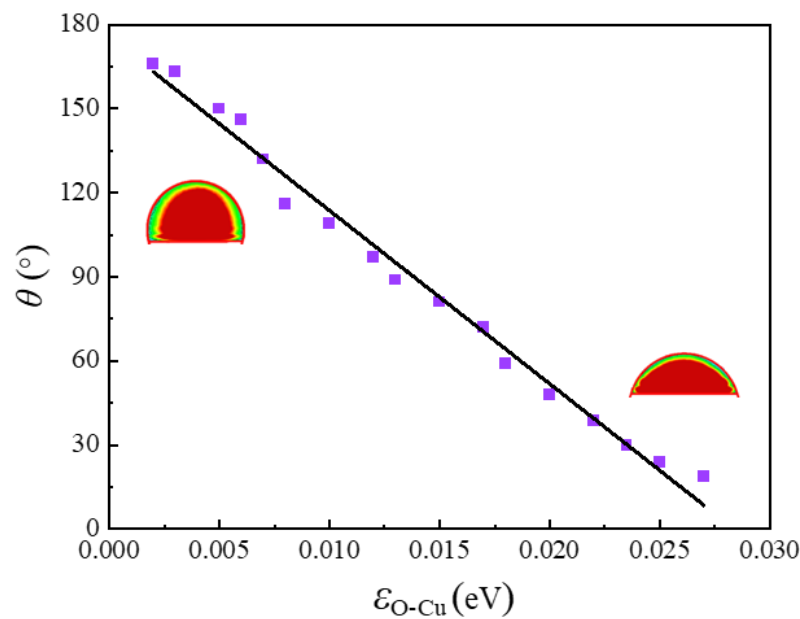
Figure 2. Relationship between θ and εO-Cu. Two density contours are given as examples of the hydrophobic and hydrophilic cases. The simulation results are shown as purple box, and the trend line is black line.

3.2. Simulation Validation

The underlying principle of the self-driving droplet on a conical curve track is like the self-driving droplet on a straight conical track, which all come from the Laplace pressure gradient [28]. Therefore, the present simulation results can be validated from two aspects. Case 100–160 was chosen as examples, as shown in Figure 3a. A straight conical track was constructed and shown as Figure 3b. A curve track with the same width was constructed and shown as Figure 3c. All the simulation details are kept the same. Snapshots of simulation results are exported and shown in Figure 3. Droplets can both move on tracks with width gradient, see cases a and b. In contrast, the droplet stays stationary on the curve track without width gradient, see case c. Therefore, the self-driving behavior of droplets on the conical curve track in the present study was verified.
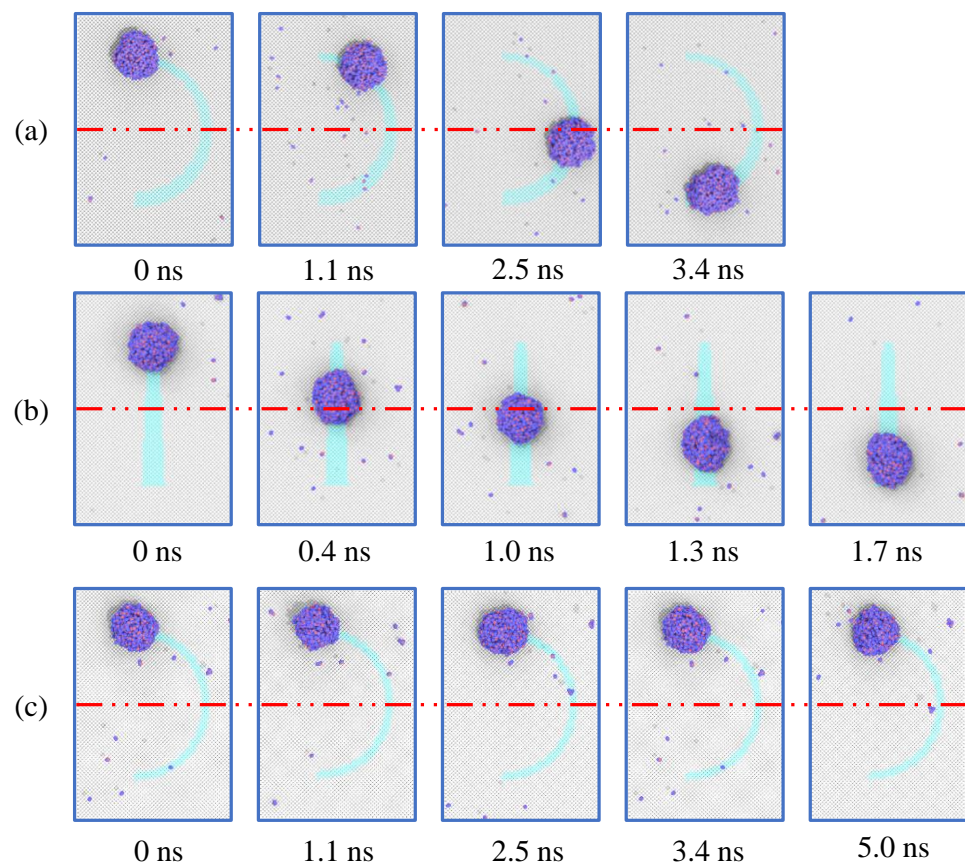
Figure 3. Snapshots of droplets on surfaces with patterns. (**a**) Curve track with width gradient. (**b**) Straight track with width gradient. (**c**) Curve track without width gradient. Red center line is marked to assist in observing droplet movement.

3.3. Theoretical Analysis

To understand the motion principle of a droplet on a curved track and its influencing factors, the model was theoretically analyzed. First, it is assumed that the droplet centroid moves on the curved track following an ideal trajectory, that is, the centerline of the curved track, as shown in Figure 4. The force equilibrium of the droplet is briefly expressed as follows:

$$F = F_L + F_W - F_H \tag{2}$$

where F_L is the Laplace pressure gradient caused by different menisci in the front and rear of the droplet along the track direction due to asymmetry of the curved track; F_W denotes the wettability gradient force generated due to the difference of the two sides of the curved track with the background in terms of wettability; F_H represents the force that resists motion of the droplet on surfaces of different wettabilities.

The droplet on the curved track is divided into four parts, in which a and b are the menisci of the droplet in the front and rear ends along the direction of motion; c and d are the droplet parts in contact with the two sides of the track, as shown in Figure 4.
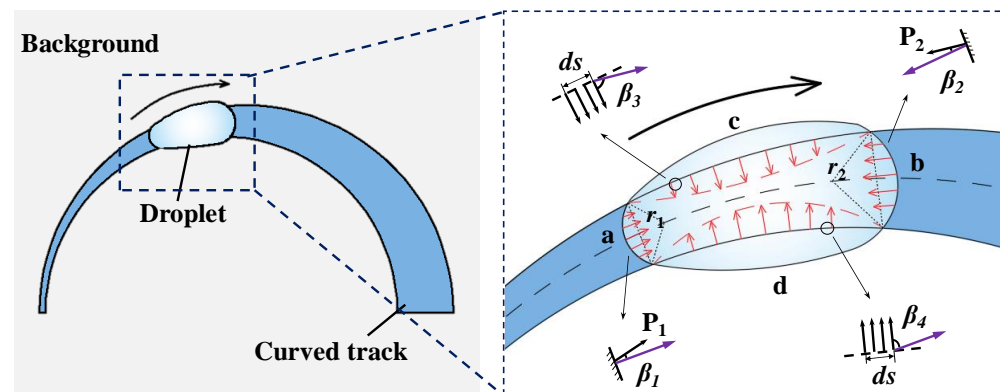
Figure 4. Theoretical model for motion of a droplet on the functional surface constituted by a gradually widening hydrophilic curved track and a hydrophobic surface.

After placing the droplet on the curved track, menisci with different radii of curvature are formed in the front and rear ends of the droplet along the direction of the curved track due to asymmetry of the hydrophilic track. Therefore, the Laplace pressure is generated, which can be expressed as follows:

$$P_1 \sim \gamma \frac{1}{r_1}, \; P_2 \sim \gamma \frac{1}{r_2} \tag{3}$$

where r_1 and r_2 separately represent the local radii of the three-phase contact line in two sides of the droplet along the track direction; γ denotes the surface tension of water.

The Laplace pressure difference acts on the droplet to drive motion of the droplet. However, the directions of P_1 and P_2 have certain angles (β_1 and β_2) with the tangential direction of the motion trajectory of the droplet due to the special shape of the curved track. The values of β_1 and β_2 are similar at any given time, so they are both replaced with β for the convenience of computation. Therefore, the resultant force along the direction of motion produced by the Laplace pressure is expressed as follows:

$$F_1 = P_1 cos\beta_1 - P_2 cos\beta_2 = 2\gamma cos\beta \left(\frac{1}{r_1} - \frac{1}{r_2} \right) \tag{4}$$

Additionally, a force normal to the direction of motion is generated by the Laplace pressure due to the presence of an angle between the force and the direction of motion.

$$F_2 = P_1 sin\beta_1 + P_2 sin\beta_2 = 2\gamma sin\beta \left(\frac{1}{r_1} + \frac{1}{r_2} \right) \tag{5}$$

The direction of action of F_2 is from side d to side c.

The driving force produced by the wettability gradient is obtained by contact areas of the droplet in the two boundary regions with different wettability. The proportional relationship between the driving force F and the contact area σ is expressed as [43]:

$$F = A \times \sigma \tag{6}$$

where A is a constant. Similarly, the wettability gradient force also has certain angles with the direction of motion of the droplet and its included angles with c and d sides are separately β_3 and β_4. Therefore, a component force vertical to the direction of motion is also generated. F_3 and F_4 that are separately vertical to the tangential direction of the motion trajectory are:

$$F_3 = \int_c A\sigma cos\beta_3 ds + \int_d A\sigma cos\beta_4 \, ds \tag{7}$$

$$F_4 = \int_c A\sigma sin\beta_3 ds - \int_d A\sigma sin\beta_4 \, ds \tag{8}$$

where the direction of action of F_4 is from c side to d side. The arc shape of the track determines that the contact area of the droplet at the boundary on the c side is larger than that on the d side. The angle difference between β_3 and β_4 is almost negligible.

Combined with the above analysis, the resultant force on the droplet in two directions is expressed as follows:

The resultant force in the direction of motion is

$$F_{\rm n} = F_1 + F_3 - F_{\rm H} = 2\gamma cos\beta \left(\frac{1}{r_1} - \frac{1}{r_2} \right) + \int_c {\rm A}\sigma cos\beta_3 ds + \int_d {\rm A}\sigma cos\beta_4 \, ds - F_{\rm H} \qquad (9)$$

The resultant force vertical to the direction of motion is

$$F_{\rm z} = F_2 - F_4 = 2\gamma sin\beta \left(\frac{1}{r_1} + \frac{1}{r_2} \right) - \int_c {\rm A}\sigma sin\beta_3 ds + \int_d {\rm A}\sigma sin\beta_4 \, ds \qquad (10)$$

Driven by $F_{\rm n}$, the droplet can move along the track; while $F_{\rm z}$ allows lateral motion of the droplet vertical to the direction of motion, which to some extent hinders the droplet motion. However, because the directions of F_2 and F_4 are opposite, the lateral motion of the droplet maintains dynamic equilibrium. Together with the adsorption of the hydrophilic track for the droplet, the droplet is always on the track. In addition, the force helps adjust the direction of motion of the droplet along the curve in the process of achieving dynamic equilibrium.

3.4. Influences of the Wettability Difference

Copper atoms were filled in the curved track region and the background region. After adding a droplet, the potential energy parameter $\varepsilon_{\rm O-Cu}$ between oxygen atoms in water molecules and copper atoms in the base was set, which controls the base to show different water wettability. In this way, a controllable wettability difference between the curve and the background by the droplet can be achieved. The wettability difference of 60 degrees was applied in the present study to save simulation resources and set different contact angle combinations.

The wettability of the curve track and background by the droplet were separately adjusted to observe and assess influences of different wetting degrees and the wettability difference on the droplet motion along the curve. The self-actuation of the droplet on three groups of surfaces with different wettability was simulated under the same wettability gradient on the track and background (the track and background have a difference of $60°$ in terms of the CA θ). These groups include: (a) the hydrophobic surface (CAs θ in the track and background separately being $100°$ and $160°$); (b) the hydrophilic-hydrophobic surface (CAs θ in the track and background separately being $60°$ and $120°$); and (c) the hydrophilic surface (CAs θ in the track and background separately being $20°$ and $80°$); (d) the hydrophobic-hydrophilic surface (CAs θ in the track and background separately being $120°$ and $60°$).

Figure 5 instantaneously illustrates droplet motion along the curve track in four groups of molecular dynamics simulations. As shown, the droplet remains quasi-ellipsoidal in the motion process in group a and group b, which is in sharp contrast to the shape of the droplet in group c. As time goes on, the droplet spreads out along the track on the hydrophilic surface and the droplet is still in the early half of the curved track. This is because when the track with stronger hydrophily is driving the droplet forward, it needs to overcome the strong pinning effect of hydrophilicity of the background on the droplet. As for case d, the droplet tends to separate from both sides of the track. The hydrophilic background surface has a larger interfacial interaction, which makes the droplets tend to spread rather than move forward, and an effective droplet driving along the curved track cannot form.
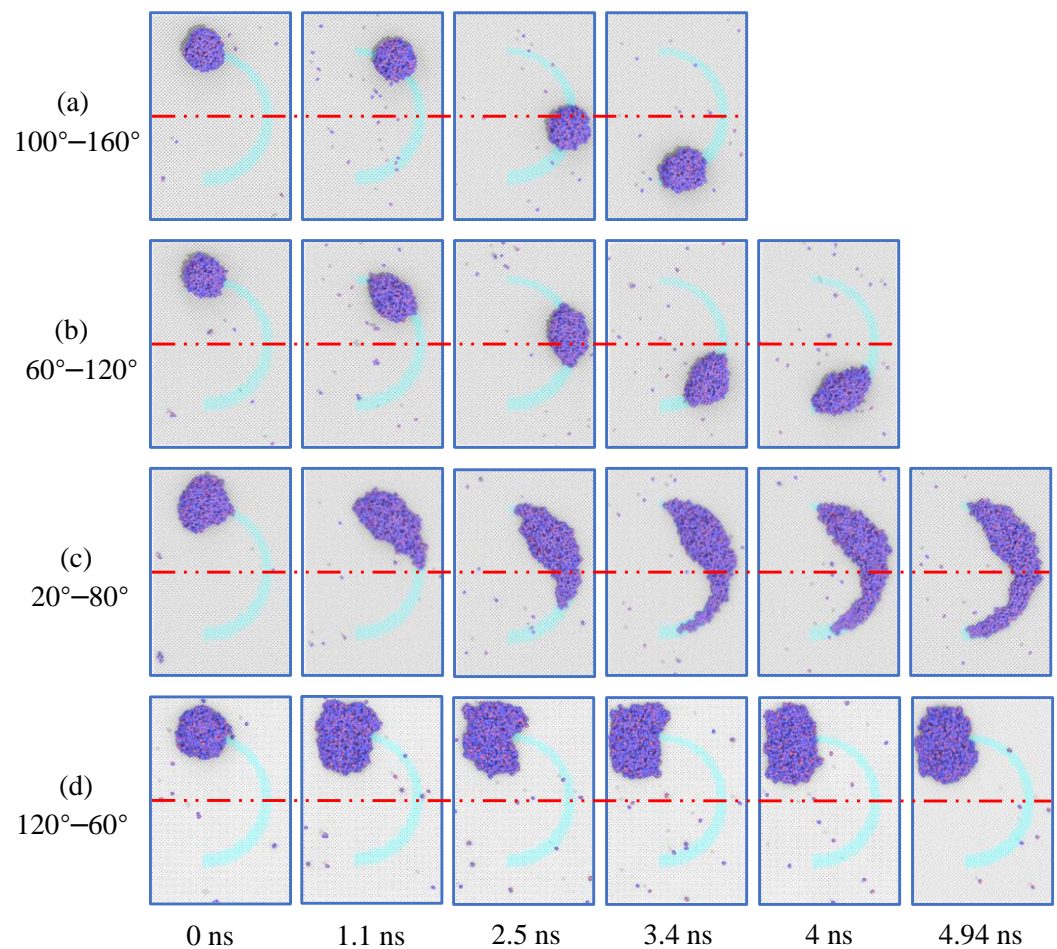
Figure 5. Instantaneous pictures for droplet motion on the curved track. (**a**) hydrophilic surface (CAs θ in the track and background separately being 100° and 160°); (**b**) hydrophilic–hydrophobic surface (CAs θ in the track and background separately being 60° and 120°); and (**c**) hydrophobic surface (CAs θ in the track and background separately being 20° and 80°); (**d**) hydrophobic–hydrophilic surface (CAs θ in the track and background separately being 120° and 60°). Red center line is marked to assist in observing droplet movement.

Data analysis indicates that the average motion velocity of the droplet in group a and group b separately reach 6.69 and 5.69 m/s, as shown in Figure 6a, while the droplet in group b moves much faster than that in group a, see Figure 6b. This is because the track and background in group a are both hydrophobic surfaces, which show weak adsorption for the droplet. In addition, the track is narrow in the initial section, which exerts slight influences on the actuating velocity of the droplet. After 1 ns, the motion velocity in group a exceeds that in group b. By observing the complete motion courses of the droplet over time in Figure 6b, the following result is found: the droplet does not always move forward on the curved track but also stagnates or, at times, retreats slightly. This is because the heading direction of the droplet constantly changes during motion on the curved track. Therefore, the forces applied by the surfaces on the droplet are also adjusted continuously in the motion process with varying directions, despite the forward motion along the track. Evidently, the self-actuation of the droplet can be realized on the functional surface and with a certain wettability difference, in which case the track and background are both hydrophobic and more conducive to the self-actuation of the droplet.
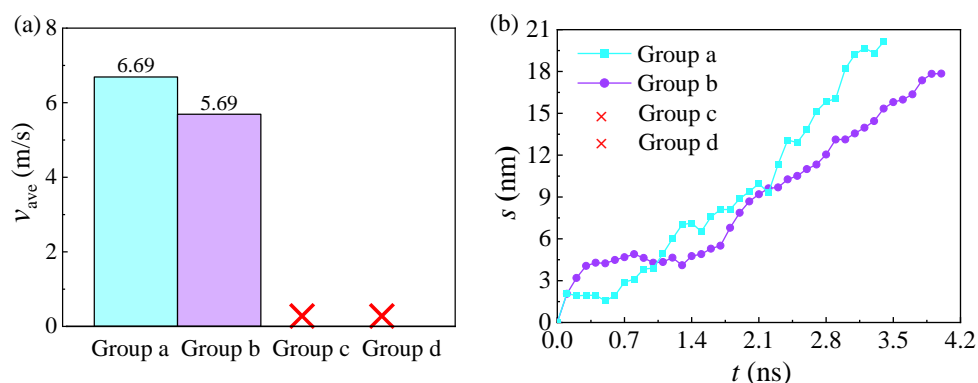
Figure 6. Influences of the wettability difference. (**a**) Average motion velocities of the droplet at varying wettability differences. (**b**) Motion courses of the droplet over time at varying wettability differences.
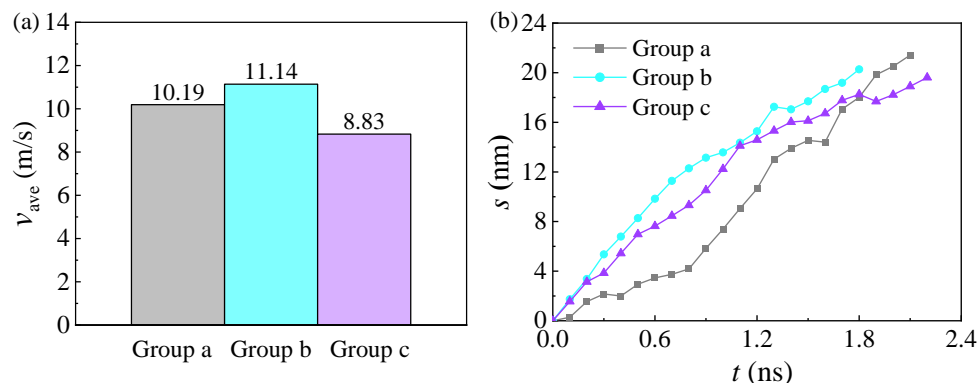
3.5. Influences of the Track Width

The hydrophobic surface (CAs θ in the track and background separately being 100° and 160°) was selected. The self-actuation performance of the droplet on the surface was simulated and observed by changing the track width. The width of the narrow end of the curved track and the radius of the cylinder 1 were kept at l_a = 3.92 Å and R_{O1} = 78.4 Å, while the radius R_{O2} of cylinder 2 was changed to 70.56, 66.64, and 62.72 Å (Figure 1), thus three groups of surfaces with different widths of the curved track.

The self-actuation of the droplet along the curve under three track widths was simulated. The instantaneous pictures for the motion are displayed in Figure 7; the curved tracks in group a, group b, and group c are narrowed in succession and the droplet separately takes 2.1, 1.82, and 2.22 ns to move from the start to the endpoint. The average motion velocities of the droplet in the three groups are 10.19, 11.14, and 8.83 m/s, respectively, see Figure 8a. After changing the track width, it can be found that, for a given initial width, the wider the track, the larger the rate of change of the track width in the direction of motion, which is more beneficial for the rapid motion of the droplet. Comparison of droplet motion in group a and group b shows that the droplet motion follows the trend; however, the droplet motion takes the longest time in group c with the widest track, corresponding to the lowest average motion velocity. Combined with analysis of Figure 8b, the motion of the droplet decelerates in the second half of the curved track. This is because the area of the most contact between the droplet and the surface is within the track as the track width increases, so that the contact area between the droplet and the more hydrophilic track enlarges, which affects the motion of the droplet. Meanwhile, the contact area between the droplet and the boundary shrinks; therefore, the driving force on the droplet is weakened, thus decelerating the motion of the droplet. The conclusion is, therefore, that an increase in the track width is conducive to the self-actuation of the droplet, while the self-actuation of the droplet is affected if the track is further widened, thus decreasing its velocity. Once the track width is larger than the spread-width of the droplet, that is, the droplet is completely within the track, the driving force on the droplet disappears, so the droplet stagnates on the track.
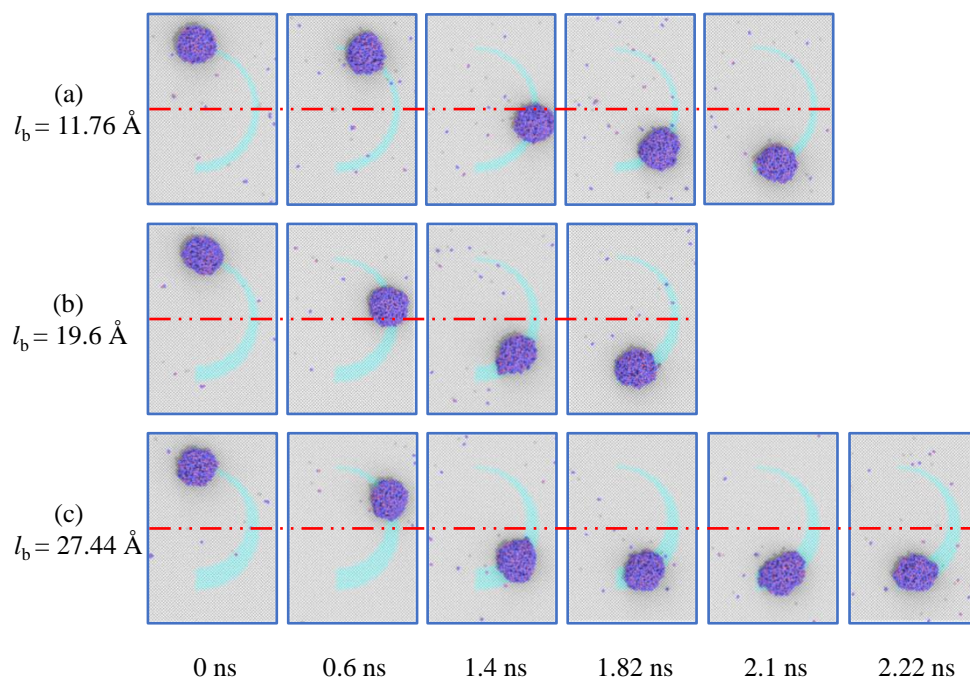
Figure 7. Instantaneous pictures showing the droplet motion on the surfaces of tracks with different widths. (**a**) The track witdh l_b is 11.76 Å; (**b**) The track witdh l_b is 19.6 Å; (**c**) The track witdh l_b is 27.44 Å. Red center line is marked to assist in observing droplet movement.


Figure 8. Influences of the track width: (**a**) Average motion velocities of the droplet correspond to different track widths. (**b**) Motion courses of the droplet over time correspond to different track widths.
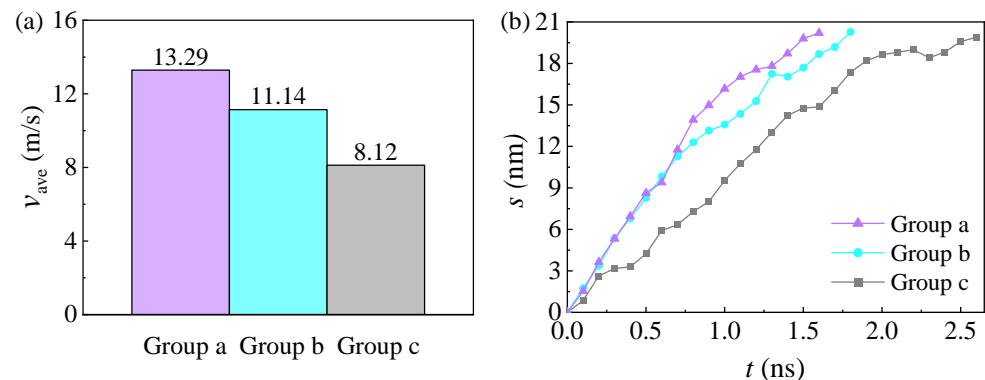
3.6. Influences of the Droplet Temperature

The temperature parameter was adjusted to explore the droplet motion on the surface at a temperature of 280, 300, and 320 K in the simulation system. The instantaneous pictures of the droplet motion along the curve at different temperatures are shown in Figure 9. The results show that the droplets move increasingly fast along the curve with rising temperature. The motion velocity of the droplet is 8.12, 11.14, and 13.29 m/s with increasing temperature, as shown in Figure 10a. The movement process of the droplet over time is shown in Figure 10b. The simulations imply that in the simulation system under different temperatures, the same potential energy parameter ε_{O-Cu} shows the same wettability of the droplet, that is, the contact angle between the droplet and the surface does not change due to different temperatures. Therefore, the analysis indicates that the motion velocity of the droplet changes mainly because the temperature change alters the intermolecular kinetic energy. As the temperature increases, molecular motion becomes more violent, thus increasing the interaction frequency of the droplet and surface and

enabling faster motion of the droplet. In practical application, the motion velocity of the droplet can be adjusted by controlling the temperature.
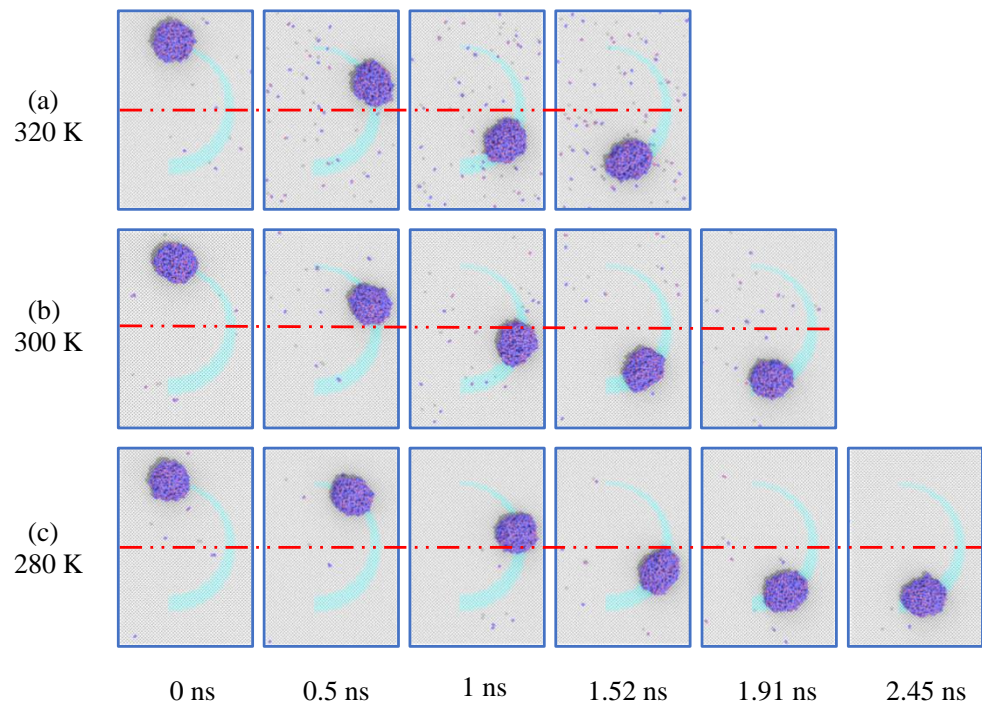
Figure 9. Instantaneous pictures of droplet motion at different temperatures. (**a**) 320 K; (**b**) 300 K; (**c**) 280 K. Red center line is marked to assist in observing droplet movement.

Figure 10. Influences of the droplet temperature: (**a**) Average motion velocity of the droplets at different temperatures; (**b**) Motion courses of the droplet over time at different temperatures.

4. Conclusions

Self-actuation of the droplet along the curve was designed and realized through molecular dynamics simulations. The motion mechanism and characteristics of the droplet on the surface were investigated. Moreover, influences of the wettability difference, the width of curved track, and the temperature on droplet motion were evaluated. The results show that:

(1) Droplet motion is achieved according to the joint action of the Laplace pressure and the wettability gradient force. The component force in the direction of motion promotes forward motion of the droplet, while the component force vertical to the direction of motion induces the droplet to turn in the direction of dynamic equilibrium. This realises droplet motion along the curved track.

(2)　Under the same wettability difference, the hydrophobic-hydrophobic combination of the curved track and the background provides a larger driving force on the droplet than the hydrophilic-hydrophobic surface and the hydrophilic-hydrophilic surface.

(3)　Increasing the width of the curved track leads to an increasingly fast motion of the droplet. However, a too large track width shrinks the contact area between the droplet and the boundary, thus decelerating the motion of the droplet and even causing the motion to stagnate. On the premise of keeping the droplet in a liquid state, the temperature rise accelerates the motion velocity of the droplet along the curved track. This is because the temperature rise increases the internal energy of molecules, leading to more violent motion, and improving the contact frequency between the droplet molecules and the surface.

The research investigates the self-actuation of the droplet along the curve from the microscopic perspective, which provides a basis for macroscopic experiments. It also reveals new opportunities for development in fields, including the lab-on-a-chip, microfluidic devices, and analytical devices using biological droplets.

Author Contributions: Methodology, Zhigang Liu; Writing—original draft, Yalong Kong; Writing—review & editing, Lin Guo and Yu Qiu. All authors have read and agreed to the published version of the manuscript.

Data Availability Statement: Not applicable.

Conflicts of Interest: The authors declare that they have no known competing financial interests or personal relationships that could appear to influence the work reported in this paper.

Nomenclature

E	The lj/cut styles compute the standard 12/6 Lennard-Jones potential
ε	Energy units
σ	Distance units
r	Interatomic spacing
r_c	Cutoff
θ	Contact angle between droplet and copper base
O_1	The center of the outer circle of the curved track
O_2	The center of the inside circle of the curved track
R_{O1}	The radius of the outer circle of the curved track
R_{O2}	The radius of the inside circle of the curve track
l_a	Narrow end distance of curved track
l_b	Wide end distance of curved track
F	The resultant force exerted by the curved track on the droplet
F_L	Laplace pressure gradient
F_W	Wetting gradient force
F_H	The force of surface with different wettability hindering the movement of droplets
P_1	Laplace pressure generated by the curved liquid surface at the rear end of the droplet along the track direction
P_2	Laplace pressure generated by the curved liquid surface at the front end of the droplet along the track direction
F_1	The force generated by Laplace pressure in the direction of droplet movement
F_2	The force generated by Laplace pressure perpendicular to the direction of droplet movement

F_3	The force generated by the wettability gradient in the direction of droplet movement
F_4	The force generated by the wettability gradient perpendicular to the direction of droplet motion
F_n	The resultant force of the droplet in the direction of the curve tracks
F_z	The resultant force of the droplet perpendicular to the direction of motion
γ	Surface tension of water
r_1	Local radius of the three-phase contact lines behind the droplet along the direction of the track
r_2	Local radius of the three-phase contact line in front of the droplet along the track direction
$\beta = \beta_1 = \beta_2$	
β_1	The angle formed by force P_1 and the direction of droplet movement
β_2	The angle formed by force P_2 and the direction of droplet movement
β_3	The angle between the c side wetting gradient force and the direction of droplet movement.
β_4	The angle between the d side wetting gradient force and the direction of droplet movement.
S	Contact area of droplets on both sides of curved track

References

1. Bixler, G.D.; Bhushan, B. Fluid drag reduction and efficient self-cleaning with rice leaf and butterfly wing bioinspired surfaces. *Nanoscale* **2013**, *5*, 7685–7710. [CrossRef]
2. Ju, J.; Bai, H.; Zheng, Y.M.; Zhao, T.Y.; Fang, R.C.; Lei, J. A multi-structural and multi-functional integrated fog collection system in cactus. *Nat. Commun.* **2012**, *3*, 1247. [CrossRef]
3. Guo, L.; Tang, G.H. Experimental study on directional motion of a single droplet on cactus spines. *Int. J. Heat Mass Transf.* **2015**, *84*, 198–202. [CrossRef]
4. Bai, H.; Ju, J.; Zheng, Y.M.; Jiang, L. Functional fibers with unique wettability inspired by spider silks. *Adv. Mater.* **2012**, *24*, 2786–2791. [CrossRef]
5. Ju, J.; Zheng, Y.M.; Jiang, L. Bioinspired one-dimensional materials for directional liquid transport. *Acc. Chem. Res.* **2014**, *47*, 2342–2352. [CrossRef] [PubMed]
6. Chen, H.W.; Zhang, P.F.; Zhang, L.W.; Liu, H.L.; Jiang, Y.; Zhang, D.Y.; Han, Z.W. Continuous directional water transport on the peristome surface of Nepenthes alata. *Nature* **2016**, *532*, 85–89. [CrossRef] [PubMed]
7. Jiao, Y.L.; Lv, X.D.; Zhang, Y.Y.; Li, C.Z.; Li, J.W.; Wu, H.; Xiao, Y.; Wu, S.Z.; Hu, Y.L.; Wu, D.; et al. Pitcher plant-bioinspired bubble slippery surface fabricated by femtosecond laser for buoyancy-driven bubble self-transport and efficient gas capture. *Nanoscale* **2019**, *11*, 1370–1378. [CrossRef] [PubMed]
8. Hamilton, W.J.; Seely, M.K. Fog basking by the Namib Desert beetle, Onymacris Unguicu-laris. *Nature* **1976**, *262*, 284–285. [CrossRef]
9. Parker, A.R.; Lawrence, C.R. Water capture by a desert beetle. *Nature* **2001**, *414*, 33–34. [CrossRef]
10. Cieplak, M.; Koplik, J.; Banavar, J.R. Nanoscale fluid flows in the vicinity of patterned surfaces. *Phys. Rev. Lett.* **2006**, *96*, 114502. [CrossRef] [PubMed]
11. Paradisanos, I.; Fotakis, C.; Anastasiadis, S.H.; Stratakis, E. Gradient induced liquid motion on laser structured black Si surfaces. *Appl. Phys. Lett.* **2015**, *107*, 111603. [CrossRef]
12. Lv, C.J.; Chen, C.; Chuang, Y.C.; Tseng, F.G.; Yin, Y.J.; Grey, F.; Zheng, Q.S. Substrate curvature gradient drives rapid droplet motion. *Phys. Rev. Lett.* **2014**, *113*, 26101. [CrossRef] [PubMed]
13. Bai, H.; Tian, X.L.; Zheng, Y.M.; Ju, J.; Zhao, Y.; Jiang, L. Direction controlled driving of tiny water drops on bioinspired artificial spider silks. *Adv. Mater.* **2010**, *22*, 5521–5525. [CrossRef] [PubMed]
14. Du, M.; Zhao, Y.; Tian, Y.; Li, K.; Jiang, L. Electrospun multiscale structured membrane for efficient water collection and directional transport. *Small* **2016**, *12*, 1000–1005. [CrossRef]
15. Hou, Y.P.; Feng, S.L.; Dai, L.M.; Zheng, Y.M. Droplet manipulation on wettable gradient surfaces with micro-/nano-hierarchical structure. *Chem. Mater.* **2016**, *28*, 3625–3629. [CrossRef]
16. Kou, J.L.; Mei, M.F.; Lu, H.J.; Wu, F.M.; Fan, J.T. Unidirectional motion of a water nanodroplet subjected to a surface energy gradient. *Phys. Rev. E Stat. Nonlin. Soft. Matter Phys.* **2010**, *85*, 988–1000. [CrossRef]
17. Wang, Z.K.; Zheng, H.Y.; Xia, H.M. Femtosecond laser-induced modification of surface wettability of PMMA for fluid separation in microchannels. *Microfluid. Nanofluid.* **2011**, *10*, 225–229. [CrossRef]
18. Gurera, D.; Bhushan, B. Multistep wettability gradient on bioinspired conical surf-aces for water collection from fog. *Langmuir* **2019**, *35*, 16944–16947. [CrossRef]

19. Chen, H.W.; Tong, R.; Yang, G.; Zhou, J.J.; Zhang, Y.; Zhang, L.W.; Zhang, D.Y.; Jiang, L. Ultrafast water harvesting and transport in hierarchical microchannels. *Nat. Mater.* **2018**, *17*, 935–942. [CrossRef]

20. Park, K.C.; Kim, P.; Grinthal, A.; He, N.; Fox, D.; Weaver, J.C.; Aizenberg, J. Condensation on slippery asymmetric bumps. *Nature* **2016**, *531*, 78–82. [CrossRef]

21. Meng, Q.A.; Xu, B.J.; He, M.J.; Bian, R.X.; Meng, L.L.; Wang, P.W.; Jiang, L.; Liu, H. Bioinspired controllable liquid manipulation by fibrous array driven by elasticity. *ACS Appl. Mater.* **2018**, *10*, 26819–26824. [CrossRef]

22. Liu, W.J.; Fan, P.X.; Cai, M.Y.; Luo, X.; Chen, C.H.; Pan, R.; Zhang, H.J.; Zhong, M.L. An integrative bioinspired venation network with ultra-contrasting wettability for large-scale strongly self-driven and efficient water collection. *Nanoscale* **2019**, *11*, 8940–8949. [CrossRef] [PubMed]

23. Li, K.; Ju, J.; Xue, Z.X.; Ma, J.; Feng, L.; Gao, S.; Jiang, L. Structured cone arrays for continuous and effective collection of micron-sized oil droplets from water. *Nat. Commun.* **2013**, *4*, 2276. [CrossRef] [PubMed]

24. Seo, K.; Kim, M.; Kim, D.H. Candle-based process for creating a stable superhydrophobic surface. *Carbon* **2014**, *68*, 583–596. [CrossRef]

25. Pei, Y.Y.; Song, Q.; Li, P. Research progress of biomimetic micro/nano-structured antibacterial surfaces. *Surf. Technol.* **2019**, *48*, 200–210. [CrossRef]

26. Lan, F.; Haliburton, J.R.; Yuan, A.; Abate, A.R. Droplet barcoding for massively parallel single-molecule deep sequencing. *Nat. Commun.* **2016**, *7*, 11784. [CrossRef] [PubMed]

27. Parashar, V.K.; Wacker, J.B.; Gijs, M.A. Spherical superstructures of oxide nanoparticles for catalytic reactions in microchemical reactors. *Mater. Lett.* **2015**, *139*, 182–186. [CrossRef]

28. Tang, X.; Huang, J.X.; Guo, Z.G.; Liu, W.M. A combined structural and wettability gradient surface for directional droplet transport and efficient fog collection. *J. Colloid Interface Sci.* **2021**, *604*, 526–536. [CrossRef] [PubMed]

29. Feng, S.L.; Wang, Q.Q.; Xing, Y.; Hou, Y.P.; Zheng, Y.M. Continuous directional water transport on integrating tapered surfaces. *Adv. Mater. Interfaces* **2020**, *7*, 2000081. [CrossRef]

30. Lin, Y.C.; Hu, Z.Y.; Gao, C.L.; Guo, Z.Y.; Li, C.; Zheng, Y.M. Directional droplet spreading transport controlled on tilt-angle pillar arrays. *Adv. Mater. Interfaces* **2018**, *5*, 1800962. [CrossRef]

31. Wang, M.; Liu, Q.; Zhang, H.R.; Wang, C.; Wang, L.; Xiang, B.X.; Fan, Y.T.; Guo, C.F.; Ruan, S.C. Laser direct writing of tree-shaped hierarchical cones on a superhydrophobic film for high-efficiency water collection. *ACS Appl. Mater.* **2017**, *9*, 29248–29254. [CrossRef] [PubMed]

32. Khoo, H.S.; Tseng, F.G. Spontaneous high-speed transport of subnanoliter water droplet on gradient nanotextured surfaces. *Appl. Phys. Lett.* **2009**, *95*, 063108. [CrossRef]

33. Zhang, J.L.; Han, Y.C. Shape-gradient composite surfaces: Water droplets move uphill. *Langmuir* **2007**, *23*, 6136–6141. [CrossRef]

34. Huang, D.J.; Leu, T.S. Fabrication of a wettability-gradient surface on copper by screen-printing techniques. *J. Micromech. Microeng.* **2015**, *25*, 1325–1336. [CrossRef]

35. Ody, T.J.; Panth, M.; Sommers, A.D.; Eid, K.F. Controlling the motion of ferrofluid droplets using surface tension gradients and magnetoviscous pinning. *Langmuir* **2016**, *32*, 6967–6976. [CrossRef] [PubMed]

36. Deng, S.Y.; Shang, W.F.; Feng, S.L.; Zhu, S.P.; Xing, Y.; Li, D.; Hou, Y.P.; Zheng, Y.M. Controlled droplet transport to target on a high adhesion surface with multi-gradients. *Sci. Rep.* **2017**, *7*, 45687. [CrossRef] [PubMed]

37. Liu, M.; Yao, Y.; Li, J.J.; Peng, Z.L.; Chen, S.H. Directional sliding behavior of a water droplet on a wedge-shape patterned functional surface. *J. Phys. Chem. B* **2020**, *124*, 6905–6912. [CrossRef] [PubMed]

38. Zheng, Y.F.; Chen, J.; Zhou, C.L.; Xing, H.T.; Wen, X.F.; Pi, P.H.; Xu, S.P. Dro-plet motion on a shape gradient surface. *Langmuir* **2017**, *33*, 4172–4177. [CrossRef] [PubMed]

39. Guan, J.H.; Élfego, R.G.; Xu, B.B.; Wood, D.; Mchale, G.; Ledesma-Aguilar, R.; Wells, G.G. Drop transport and positioning on lubricant-impregnated surfaces. *Soft. Matter* **2017**, *13*, 3404–3410. [CrossRef] [PubMed]

40. Zhang, C.H.; Zhang, B.; Ma, H.Y.; Li, Z.; Xiao, X.; Zhang, Y.H.; Cui, X.Y.; Yu, C.M.; Cao, M.Y.; Jiang, L. Bioinspired pressure-tolerant asymmetric slippery surface for continuous self-transport of gas bubbles in aqueous environment. *ACS Nano* **2018**, *12*, 2048–2055. [CrossRef]

41. Bai, H.; Wang, L.; Ju, J.; Sun, R.Z.; Zheng, Y.M.; Jiang, L. Efficient water collection on integrative bioinspired surfaces with star-shaped wettability patterns. *Adv. Mater.* **2014**, *26*, 5025–5030. [CrossRef] [PubMed]

42. Wang, S.; Wang, C.; Peng, Z.L.; Chen, S.H. Moving behavior of nanodroplets on wedge-shaped functional surfaces. *J. Phys. Chem. C* **2019**, *123*, 1798–1805. [CrossRef]

43. Xu, B.; Chen, Z.Q. Droplet movement on a composite wedge-shaped surface with multi-gradients and different gravitational field by molecular dynamics. *Microgravity Sci. Tec.* **2018**, *30*, 571–579. [CrossRef]

44. Hao, S.Q.; Xie, Z.; Li, Z.; Kou, J.L.; Wu, F.M. Initial-position-driven opposite directional transport of water droplet on wedge-shaped groove. *Nanoscale* **2021**, *13*, 15963–15972. [CrossRef]

45. Guo, L.; Kumar, S.; Yang, M.Y.; Tang, G.H.; Liu, Z.G. Role of the microridges on cactus spines. *Nanoscale* **2022**, *14*, 525–533. [CrossRef]

46. Mo, J.W.; Wang, C.; Zeng, J.Y.; Sha, J.J.; Li, Z.G.; Chen, Y.F. Directional passive transport of nanodroplets on general axisymmetric surfaces. *Phys. Chem. Chem. Phys.* **2022**, *24*, 9727–9734. [CrossRef] [PubMed]

47. Tan, X.H.; Zhu, Y.Y.; Shi, T.L.; Tang, Z.R.; Liao, G.L. Patterned gradient surface for spontaneous droplet transportation and water collection: Simulation and experiment. *J. Micromech. Microeng.* **2016**, *26*, 115009. [CrossRef]

48. Halverson, J.D.; Maldarelli, C.; Couzis, A.; Koplik, J. A molecular dynamics study of the motion of a nanodroplet of pure liquid on a wetting gradient. *J. Chem. Phy.* **2008**, *129*, 827. [CrossRef] [PubMed]

49. Huang, Q.J.; Zhang, Z.Q.; Liu, Z.; Zhang, F.J.; Cheng, G.G.; Ding, J.N. Pinning effect in droplet self-driving and its reduction mechanism by monolayer graphene. *Appl. Surf. Sci.* **2021**, *542*, 148666. [CrossRef]

50. Zhang, Z.Q.; Guo, X.F.; Tang, H.Y.; Ding, J.N.; Zheng, Y.G.; Li, S.F. Unidirectional self-driving liquid droplet transport on a monolayer graphene-covered textured substrate. *ACS Appl. Mater.* **2019**, *11*, 28562–28570. [CrossRef] [PubMed]